ADVANCED FUNCTIONAL MATERIALS
www.afm-journal.de

Strain-Insensitive Pre-Stretch-Stabilized Polymer/Gold Hybrid Electrodes for Electrochemiluminescent Devices

Ziyu Chen, Runhui Zhou, Jiaoya Huang, Huichen Xu, Zemin Li, Yushu Wang, Rongrong Bao, Jiang He,* and Caofeng Pan**

The quest for stretchable properties is at the forefront of research dedicated to on-skin light–emitting devices. Inspired by the natural wonders of bioluminescence, electrochemiluminescent devices (ECLDs) are distinguished by straightforward design and reduced operating voltage, marking a departure from traditional current-driven electroluminescent devices (ACELDs). The primary challenge of fully-stretchable ECLDs lies in crafting electrodes that simultaneously satisfy the demands for conductivity, transparency, stretchability, oxidation resistance, and interface stability. This research introduces a groundbreaking wrinkled polymer-gold composite electrode. It extends to 50% stretchability, offers outstanding conductivity at 10 Ω sq^{-1}, achieves transparency above 60%, and withstands over 10 000 stretching cycles. Employing this material, alongside stretchable electrospinning fiber luminescent layers, enabled the creation of fully-stretchable ECLDs. These devices not only shine brightly at 30 Cd m^{-2} but also retain more than 90% of luminosity when stretched up to 50%. Furthermore, this work has engineered stretchable devices featuring singular patterns and multi-dot arrays. They exhibit consistent luminescent output under bending, twisting, and stretching when applied to skin. These findings not only highlight the potential of polymer-gold composite electrodes in overcoming challenges faced by stretchable electronic devices but also provide new ideas for wearable technology that seamlessly integrates with human body.

1. Introduction

With the growth of demand and technological advances,[1] light–emitting display devices have developed from rigid to flexible and stretchable,[2] finding widespread applications in human-computer interaction, motion monitoring, medical and healthcare, and intelligent communication.[3] These devices utilize transient luminescence to transmit signals and achieve visual effects.[4] As components of fully-stretchable light–emitting display devices, high requirements are put forward for both the electrode layer and the light–emitting functional layer. Specifically, stretchable electrodes need to exhibit a delicate balance between conductivity, transparency, and stability.[5] The percolation threshold determines the formation of interconnecting conductive networks, and the deposition of ultrathin metals facilitates efficient carrier injection.[6] The film thickness of the continuously deposited metal creates a contradiction with high transparency.[7] Additionally, the optoelectronic properties of the luminescent functional layer are desired to be optimized, as well as modulus matching between layers to prevent delamination.[8] Realizing devices that combine all these characteristics remains a challenge.

At present, numerous studies have been conducted to solve the problems. For example, research has already focused on organic/quantum light–emitting diodes (OLEDs/QLEDs).[9] They combine flexible substrates that provide mechanical compliance with rigid LEDs. This approach may require additional carrier injection and transport layers, and the complexity of multilayer structures hinders cost-effective and large-scale manufacturing. The alternating current-driven electroluminescent device (ACELD) is also a typical fabrication strategy.[10] Textile-shaped ACELDs show large-area displays with functionality.[11] Also, EL devices can be manufactured with high compatibility and enhanced interlayer adhesion using custom 3D printed inks.[12] However, the operation at high voltages and consumption of more energy presents safety and power concerns. In that case, a novel AC-driven electrochemiluminescent device (ECLD) was prepared.[13,14] In contrast to OLED/QLED and ACELD, ECLD exhibits a simplified structure comprising an electrode layer and

Z. Chen, H. Xu, Y. Wang, C. Pan
Center on Nanoenergy Research
Institute of Science and Technology for Carbon Peak & Neutrality; Key Laboratory of Blue Energy and Systems Integration (Guangxi University)
Education Department of Guangxi Zhuang Autonomous Region
School of Physical Science & Technology
Guangxi University
Nanning 530004, China
E-mail: pancaofeng@buaa.edu.cn
Z. Chen, R. Zhou, J. Huang, Z. Li, R. Bao, J. He
Beijing Institute of Nanoenergy and Nanosystems
Chinese Academy of Sciences
Beijing 101400, China
E-mail: baorongrong@binn.cas.cn; hejiang@binn.cas.cn
C. Pan
Institute of Atomic Manufacturing
Beihang University
Beijing 100191, China

The ORCID identification number(s) for the author(s) of this article can be found under https://doi.org/10.1002/adfm.202406434

DOI: 10.1002/adfm.202406434

a light–emitting layer.[15] ECLD operates at a significantly lower voltage, enabling normal functionality through excitation below 10 V.[16] Additionally, ECLD electrodes are not constrained by power function limitations and can be manufactured cost-effectively on a large scale. These advantages position ECLD as a promising candidate for the implementation of stretchable luminescence. Several studies have explored applications in ECLD displays, preparing wearable pressure-sensitive light–emitting sensors,[17] ion gel-based flexible full-color displays.[18] For the selection of electrode materials, silver nanowires (AgNWs) have excellent flexibility and conductivity. However, their high surface roughness and vulnerability to oxidation make them unsuitable for ECLD.[19] ITO can achieve higher transmittance, yet the rigidity limits the fabrication of stretchable devices. Almost all electrodes used for ECLDs can only be flexible or partially stretchable, making them difficult to achieve fully-stretchable.[20,21]

Intrinsically stretchable devices contribute to improved stretch stability, mechanical robustness, and biocompatibility.[22] To achieve high-performance fully-stretchable ECLDs, various issues such as material selection, microstructure design, fabrication processes, and system integration need to be addressed.[23,24] Thin-layer Au combines high conductivity, great transparency, ductility, and chemical inertness, making it an ideal solution for ECLD to replace ITO and Ag as electrode materials.[25] The structure of ECLD generally consists of an electroluminescent functional layer embedded in two structurally designed electrode layers. In terms of electrode microstructure, they are carefully designed to distribute mechanical strain and reduce damage to the intermediate layer. Taking the pre-stretch-release method as an example,[26,27] when releasing the strain, the upper conductive material experiences compression and deformation by the lower elastomeric substrate. This results in the relaxation of the composite material to its original length, leading to the reorganization of the wavelength and amplitude of waveforms while minimizing energy consumption. At last, a conformal sinusoidal wrinkled structure can be given. During the fabrication process, it's necessary to consider the modulus matching of each layer and the adhesion of soft-hard interfaces to prevent delamination.[28]

Here, we report the preparation of fully-stretchable devices using electrochemical reactions for light–emitting displays and wearable sensing. ECL displays are based on a simple device structure and operation mechanism consisting of thin-layer electrodes and light–emitting layers. The electrodes are prepared via the pre-stretch-release method, resulting in a wrinkled structure after release, which can operate continuously for over 10000 cycles. The vapor-deposited parylene serves as an intermediate layer to address the issue of modulus matching between the metal conductive material and the polymer substrate. This ensures the relative resistance stability during stretching. Notably, the red and green band transmittance levels surpass 60%, accompanied by a low surface resistance of less than 10 Ω sq^{-1}. The luminescent layer based on electrospinning fibers uniformly infiltrates the luminescent solution, enabling red and green color luminescence with optoelectronic performance superior to traditional gel electrolyte luminescent layers. Fully-stretchable ECLDs were successfully fabricated with strong interlayer adhesion and resistance to delamination during stretching, resulting in a luminous brightness of 30 Cd m^{-2}. Furthermore, the ECLD exhibits consistent luminescence performance in the degree of stretching more than 40%, maintaining over 80% of its original brightness after 500 cycles. The stretchable effect of single patterns and multi-dot arrays allows for adherence to human skin and a stable luminescent display that follows bending, twisting, and other movements.

2. Results and Discussion

2.1. Design of the Electrodes via Pre-Stretch-Release Method

We envision the ECLD application scenario as shown in **Figure 1**. The ECLD is applied to the human skin for daily activities. It can maintain normal light emission during twisting and stretching motions such as clenching the fist, extending the arm, and flipping the wrist. It comprises an electrospinning luminescent layer embedded in two layers of pre-stretched gold-plated electrodes.

The electrodes were fabricated as flexural fold structures through the pre-stretch-release method. The amplitude of the fold waveforms decreased progressively during stretching and the overall shape gradually flattened until returning to the initial pre-stretching degree. The fabrication procedure is illustrated in **Figure 2a**. The VHB was adhered to the PDMS film using glue, resulting in the formation of a tightly bonded structure upon curing. Subsequently, a parylene layer was deposited via chemical vapor deposition (CVD) and a thin layer of gold was applied using magnetron sputtering. Following the strain release of the pre-stretched film, the metal-polymer multilayer composite, specifically PDMS/VHB/Parylene/Au, formed a wavy folded structure from the bottom up. VHB acts as the substrate onto which the metal and polymer are directly deposited. Therefore, we used PDMS to form a tightly bonded structure with VHB to avoid the effect of the larger viscoelasticity. Parylene is a biocompatible, chemically inert, optically transparent polymer with low gas and water permeability. The thermal and mechanical properties allow Parylene films to be used as an intermediate layer to mitigate the performance mutation at the interface between Au and PDMS/VHB.[8] Figure S1 (Supporting Information) illustrates the cross-section and surface morphology of the electrodes.

2.2. Growth of Thin Gold Film

The deposition of thin layers of gold, depicted in Figure S2 (Supporting Information), is accomplished through a two-stage process involving nucleation and nucleation-centered growth. Gold exhibits a low surface resistance attributed to its elevated free electron density relative to conductive composites. In the initial phase of film deposition, the distribution of metal atoms is influenced by the interaction: i) metal adatom and adjacent metal adatom, ii) metal adatom and substrate adatom. Depending on the magnitude of the forces between them, there are three possible modes of growth.[5,6] i) If the interaction between metal adatom and adjacent metal adatom is larger than the interaction between metal adatom and substrate adatom, the wettability of the metal adatom with the substrate is poor, leading to nucleation and growth following the Volmer-Weber mechanism (island). Then the isolated 3D island-like structures were formed

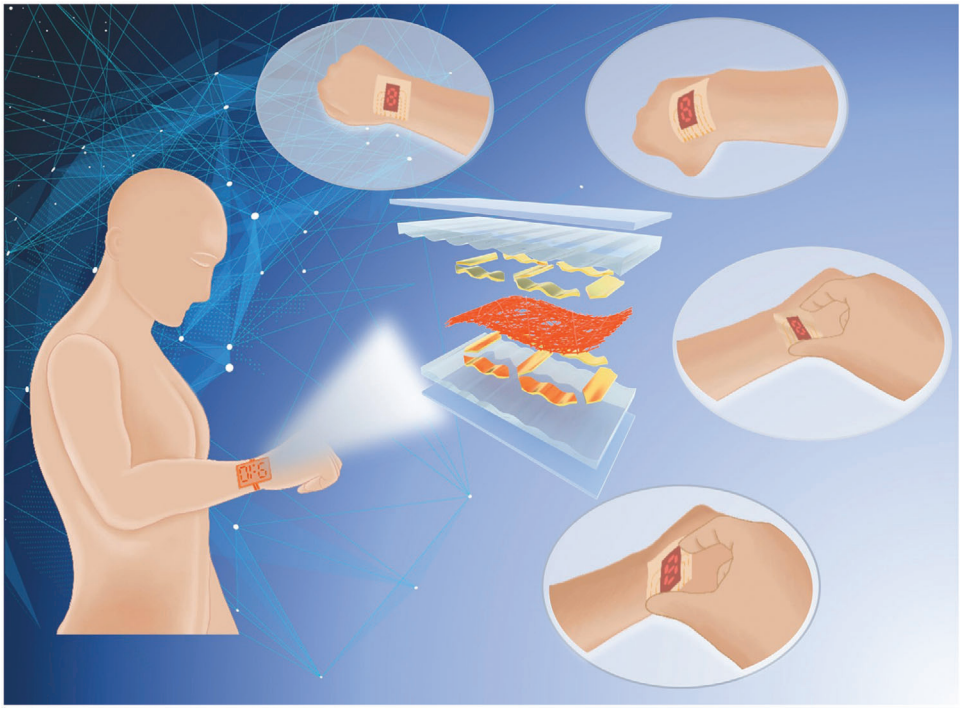

Figure 1. Design of electrochemiluminescence devices (ECLD).

on the substrate. ii) When the interaction between metal adatom and substrate adatom is gradually increased, the transition to the Stranski-Krastanov mechanism (layer-island) begins. At this point the deposition process initially exhibits itself through the formation of one or two layers of material, resulting in a modification of the surface energy of the film. As the metal is deposited, the higher surface energy tends to cause subsequent growth to follow the Volmer-Weber mechanism. As a result, isolated islands on top of the layers appeared. iii) When the interaction between metal adatom and substrate adatom continues to increase beyond the interaction between metal adatom and adjacent metal adatom, the Frank-Van der Merwe mode (layer-by-layer) is initiated.

According to the analysis above, non-uniform nucleation occurs during the vapor deposition of a thin layer of gold, resulting in uneven distribution of nucleation sites and disordered growth around these sites. The initial surface morphology of the deposition process is illustrated in Figure 2b. After 15 s of gold plating, it shows discontinuous dispersed island and granular structures, hindering the formation of a conductive network. To improve electrical conductivity, the deposition time needs to be increased. The isolated islands can be linked together, as evidenced by the surface morphology at 30 s of gold plating. While this strategy does lead to a notable enhancement in electrical conductivity, longer deposition times yield thicker gold layers that possess high reflectivity and modulus, rendering them less transparent and flexible. This limits their suitability for use as stretchable electrodes. Thus, precise control of the deposited thickness is essential to achieve higher transmittance in the near-infrared and visible spectra, thereby addressing the drawbacks associated with thick-layer metals.

One approach to regulating deposition time involves surface modification. In terms of metal deposition growth modes, the manipulation of interfacial properties is crucial in inhibiting the Volmer-Weber growth mechanism and reducing the penetration threshold. Specifically, for the electrode structure, direct adhesion of Au to the VHB surface is inadequate, leading to delamination during stretching. Therefore, an intermediate transition layer is necessary to address the modulus mismatch between metal and substrate. The incorporation of Cr is beneficial for improving adhesion, although its susceptibility to brittle cracking during stretching should be considered. In the realm of polymers, parylene films exhibit notable characteristics such as high strength, favorable biocompatibility, chemical inertness, and interfacial stability with metals. The growth of parylene films involves the utilization of chemical vapor deposition (CVD) technology, wherein small polymer molecules are deposited onto the surface of a substrate to form a fully conformal polymer film coating. With Young's modulus of 3.2 GPa, parylene falls within the range of mechanical properties between VHB (0.26 MPa) and gold (79 GPa), thereby serving to mitigate the abrupt transition in mechanical properties between these two materials. During the process of stretching, the Young's modulus-matched polymer substrate suppresses localized strains and achieves greater strain at break. Figure 2c shows the results after surface modification by parylene plating. This modification significantly enhances the adhesion of gold, with fewer cracks and voids on the plated surface at the same time (compared to Figure 2b). These findings suggest that the modified substrate surface significantly improves the interaction with gold, resulting in the formation of a dense film that covers nearly the entire surface after just 30 s of gold plating. It can also be seen in Figure 2d at the

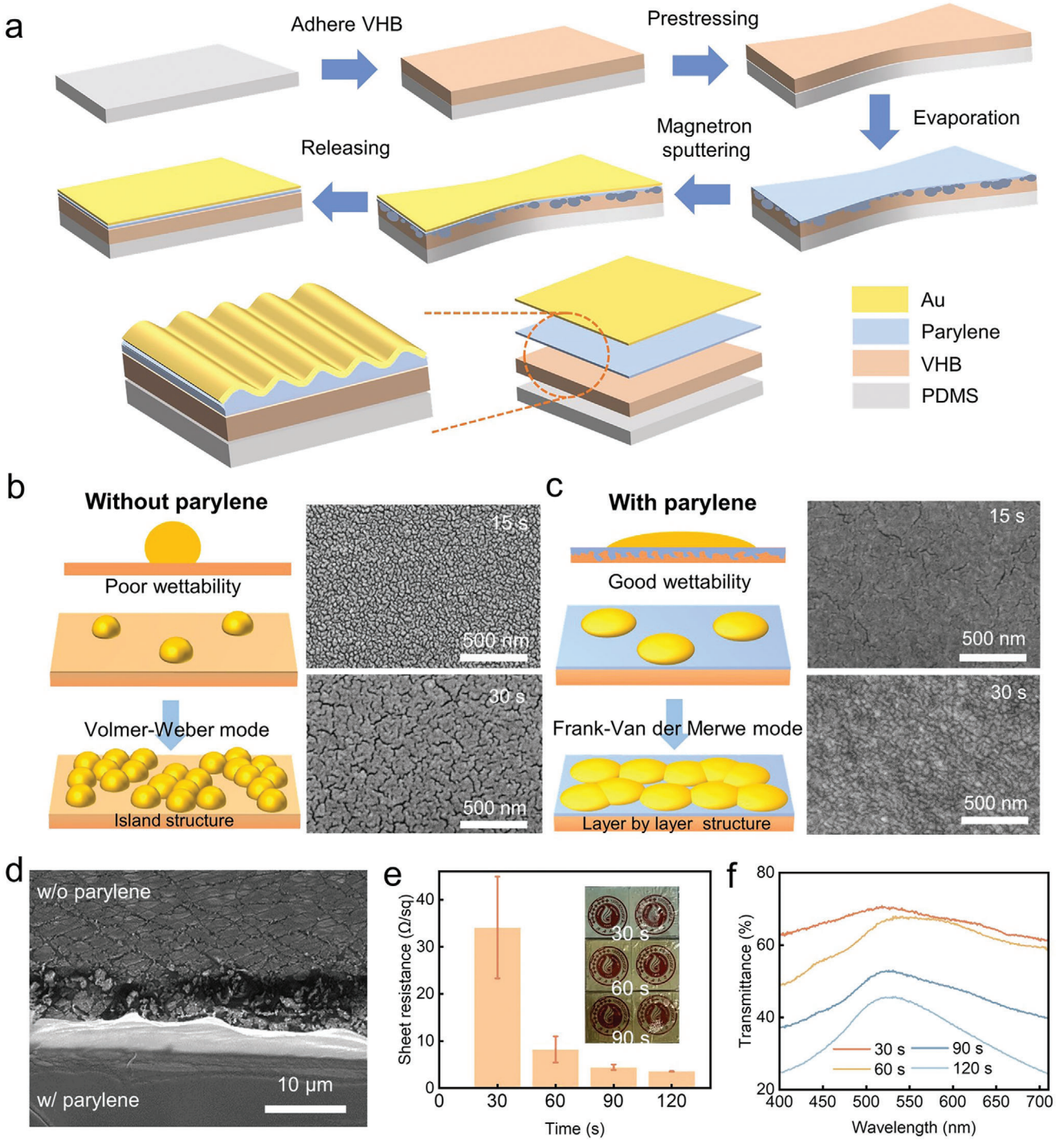

Figure 2. Preparation of stretchable electrodes. a) Schematic of the fabrication process of the pre-stretched wrinkled electrodes. Schematic and SEM images of the Au-VHB deposited films under different gold plating times b) w/o and c) w/ parylene. d) SEM images of the Au-VHB deposited films (top: w/o parylene and bottom w/ parylene). e) Sheet resistance and f) transmittance of Au-parylene-VHB films by magnetron sputtering with different gold plating times, along with corresponding sample images in inset (left: w/ parylene and right: w/o parylene).

interface of no parylene plating (top) and parylene plating (bottom) to see the difference between the surfaces of the two regions. These morphologies are further evidence of a shift in the growth mode of thin-layer gold deposition. Next, surface resistance was measured for varying plating durations, as shown in Figure 2e. The square resistance steadily decreases from over 30 Ω sq^{-1} after 30 s of gold plating. Further extension of the gold plating duration beyond 60 s shows minimal impact on the extent of the decrease in surface resistance. The inset is optical images of samples with different plating times, with the top-to-bottom

progression indicating an increase in plating time. The school logo of "Guangxi University" is discernible in the background when observed through the electrode. From left to right, the electrodes are plated with and without parylene, and the thin layer of gold on top of the parylene-coated layer is smoother and flatter. Analysis of the light transmittance of the gold-plated electrodes (Figure 2f; Figure S3, Supporting Information) reveals that electrodes plated for 60 s exhibit a transmittance exceeding 60% in the red and green light spectrums, rendering them semi-transparent. Based on these results, shorter plating times do not yield significant improvements in transmittance. Conversely, longer plating times initially result in a substantial decrease in transmittance, falling below 50%. By considering both electrode surface resistance and transmittance properties, an optimal plating time of 60 s was determined for the subsequent preparation of electrodes.

2.3. The Wrinkled Structure

As a common method of forming flexural structures, the pre-stretch-release method generally involves the deposition of high-modulus inelastic conductive films on a pre-stretched low-modulus elastic substrate. When parylene with GPa-level modulus is deposited directly on a pre-stretched VHB with a lower modulus of MPa-level, the composite tends to form a sinusoidal wave shape film during relaxation to dissipate the mechanical strain. Subsequently, the gold deposited on top of the composite forms a tightly adherent folded structure. The progressive elongation of the electrodes from their initial length to the predetermined pre-stretch level is illustrated in **Figure 3a**. After the electrodes were stretched uniaxially to a pre-stretch level of 50% and returned to their original length, then random folds emerged, predominantly perpendicular to the direction of pre-stretching. As the extension continued within the pre-stretching range, the undulating flexure structure underwent gradual stretching and flattening. At the same time, the structure retained its interconnected percolation network, thereby maintaining superior electrical characteristics even under higher strains. Figure S4 (Supporting Information) shows the wavelength statistics observed during the stretching process. The center wavelength gradually increases, reaching only a few tens of micrometers. This limited increase in wavelength prevents the occurrence of larger wavelengths in the range of a few hundred microns, which are perceptible to the naked eye and can result in macroscopic visual distortion. Exceeding the pre-stretching degree may result in the disruption of the conductive pathway, impacting the functionality of the material as an electrode. Consequently, the degree of pre-stretching determines the actual elongation. In order to assess the impact of parylene as an intermediary layer, we compared the tensile effect of electrodes without parylene, i.e., wrinkled PDMS/VHB/Au, as shown in Figure S5 (Supporting Information). In the absence of parylene, cracks developed on the surface of the pre-stretched electrodes upon restoration to their original length. Under uniaxial stretching, the cracks extended parallel to the stretching direction until reaching a 40% stretching rate. At this point, the cracks began to close, but still visible. The existence of cracks in the percolation network influences its integrity and has a notable effect on electrical conductivity. It is evident that the incorporation of an intermediate layer is essential for dispersing mechanical strain, enhancing interfacial adhesion, and promoting modulus matching between the layers.

In the context of the pre-stretch-release method, linear folds are generated through uniaxial pre-stretching, demonstrating periodicity in the direction of stretching.[24,26] The fundamental characteristics, including shape, wavelength, and amplitude of the resulting flexure structure, are contingent upon the Young's modulus, Poisson's ratio, thickness, and level of pre-stretching (ϵ_{pre}). The initial wavelength λ_0 can be expressed by the following equation:

$$\lambda_0 = 2\pi h\left(\frac{\overline{E_f}}{3\overline{E_s}}\right)^{\frac{1}{3}} \tag{1}$$

$$\overline{E_f} = \frac{E_f}{1-V_f^2} \tag{2}$$

$$\overline{E_s} = \frac{E_s}{1-V_s^2} \tag{3}$$

where h is the thickness of the top layer with the elastic modulus E_f and Poisson's ratio V_f, which is located on a substrate pre-strained with the elastic modulus E_s and Poisson's ratio V_s, respectively. Considering the potential delamination or nonlinear stress-strain behavior of the material on the stretchable elastic substrate, the initial wavelength λ and ϵ_{pre} are closely intertwined. The wavelength equation can be further described as:

$$\lambda = \frac{\lambda_0}{\left(1+\epsilon_{pre}\right)\left(1+\xi\right)^{\frac{1}{3}}} \tag{4}$$

$$\xi = \frac{5}{32}\,\epsilon_{pre}\left(1+\epsilon_{pre}\right) \tag{5}$$

λ is found to be inversely related to ϵ_{pre} based on the derivation. The electron micrographs, wavelength statistical distributions, and Gaussian fitting curves presented in Figure S6 (Supporting Information) support these results. Various periodic fold structures were observed for different ϵ_{pre}, with λ decreasing gradually as ϵ_{pre} increased from 10% to 30% and 50%. A higher stretching rate results in a more pronounced shrinkage of the entire film. In consideration of the constrained intrinsic stretchability of the VHB/PDMS substrate, the parameter ϵ_{pre} (0% to 50%) was constrained to prevent delamination and maintain control over the wavelengths and shapes. Figure 3b illustrates the fluctuation in relative resistance of the films under various stretching rates. Samples coated with parylene at varying ϵ_{pre} levels maintain stable relative resistance within their designated pre-stretched intervals, occasionally surpassing the predetermined range. In sharp contrast, the sample with ϵ_{pre} of 50% and uncoated parylene experiences challenges in maintaining an effective percolation network of Au during stretching. We stretched the film from 0% to 55% in 5% steps and then back to the original length to form a stepped load for the stretching cycle test (Figure S7, Supporting Information). Consequently, we have effectively fabricated stretchable electrodes for applications. As illustrated in Figure 3c,

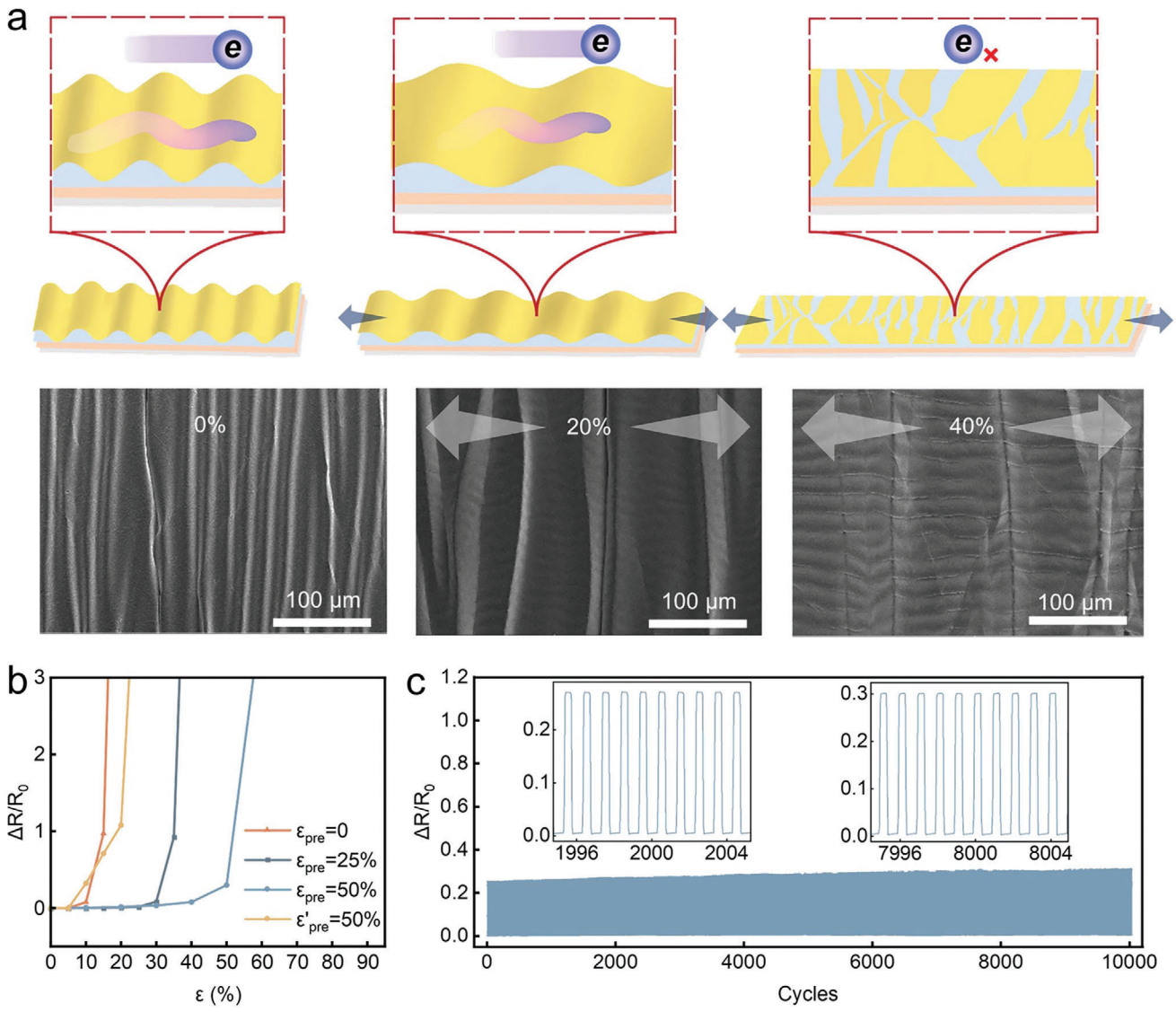

Figure 3. The stretchable performance of wrinkled Au-parylene-VHB electrodes. a) Schematic and SEM images of the pre-stretched wrinkled electrodes under different strains from 0% to 40%. b) Normalized resistance changes of different pre-stretched electrodes as a function of strain. c) Stability of the relative resistance changes of electrodes over 10000 stretching cycles at a strain of 40%.

the electrodes demonstrate resilience to over 10000 consecutive strain cycles at 40% stretching, with minimal change in relative resistance.

2.4. Fabrication and Luminescence Principle of ECLD

Figure 4a,b depicts schematic diagrams illustrating the preparation and structure of the ECLD. It is characterized by a sandwich structure comprising an electrospinning luminescent layer embedded between two layers of pre-stretched electrodes. Specifically, the luminescent layer is composed of an electrospinning Thermoplastic Polyurethane (TPU) film infused with a luminescent solution. It contains a red luminophore $[Ru(bpy)_3](PF_6)_2$, a green luminophore $[Ir(diFppy)_2(bpy)]PF_6$, dissolved in acetone, and an ionic liquid [EMIM][TFSI] that facilitates the generation of ECL. The porous structure depicted in the SEM image (Figure 4c) serves as a supportive framework to enhance the incorporation and permeation of the solution. The luminescent solution was evenly distributed within the electrospinning layer.

In conventional practice, the preparation of the luminescent layer's morphology typically involves the spin-coating of an electrolyte gel. However, challenges related to interfacial adhesion may arise during stretching. To address this issue, we initially applied the TPU gel layer onto the glass using the spin-coating technique. The performance of the electrospinning layer on PET was evaluated in comparison to the performance of the reference (Figure S8a, Supporting Information). The luminophores exhibited a more uniform distribution within the electrospinning layer. The spin-coated electrolyte gel displayed potential drawbacks such as uneven and uncontrollable thickness. The thin gel layer was found to be prone to breakage and challenging to

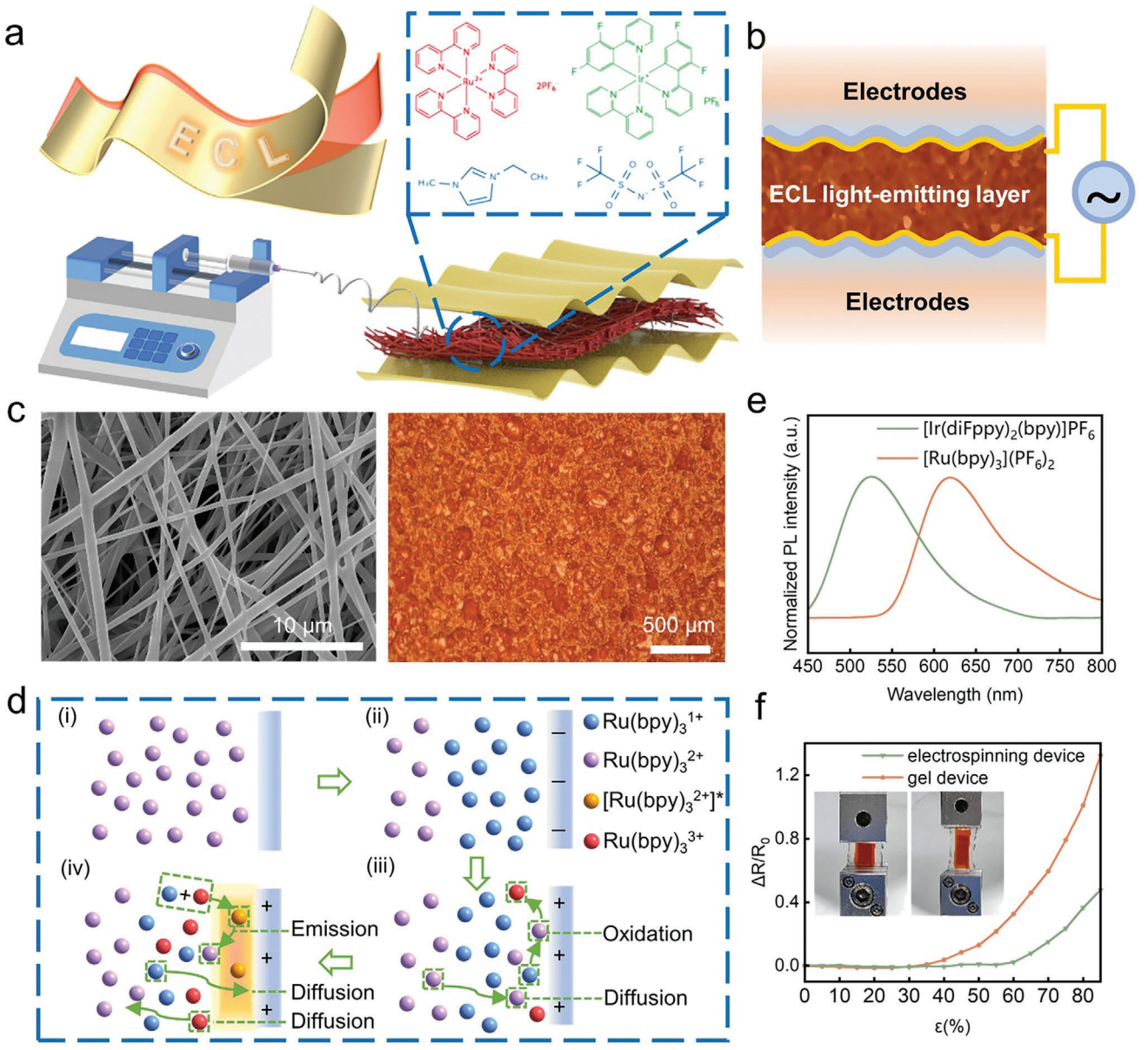

Figure 4. Fabrication and luminescence principle of ECLD. a) Fabrication of ECLD. (b) The structure of ECLD. c) The SEM images of TPU layer and optical microscope of ECL light–emitting layer (red) based on electrospinning. d) Principles of ECL. e) PL spectrum of red and green ECL light–emitting layer. f) Normalized resistance changes of the pre-stretched ECLD with electrospinning and gel as a function of strain.

remove, while the thick gel layer struggled to securely adhere to the electrode layer due to the tendency of TPU gel to be dry, impacting the conformal contact between the two layers. Figure S8b (Supporting Information) displays the optical microscope image of the green electrospinning luminescent layer, exhibiting a higher concentration of precipitated particles compared to the red luminescent layer. It is attributed to the elevated concentration of the luminescent solution, which makes it difficult to dissolve all the luminescent bodies. Furthermore, the incorporation of PEG into the luminescent solution serves to enhance luminescence performance by acting as an electrolyte with effective moisturizing properties. In Figure S9 (Supporting Information), an increase in the percentage of PEG in the luminescent solution results in a significant improvement in brightness, particularly at ≈10 wt.% of PEG making the luminescent brightness increase by more than three times. However, an excessive amount of PEG diminishes the percentage of luminescence and impacts the overall brightness. Consequently, a PEG percentage of 10 wt.% was determined, and solutions with varying luminophore contents were prepared to assess luminescence performance and optimize solution ratios for enhanced brightness. The device utilizes direct bonding of the electrode layer and light–emitting layer through the adhesion of VHB, eliminating the need for an additional spacer layer. As a result, we obtained ECLDs utilizing red and green light–emitting layers, designated as ECLD-R and ECLD-G, respectively.

The prepared ECLDs can be activated to emit light with an AC bias voltage of 10 V or lower. The luminescence of ECLDs is primarily driven by redox reactions. Taking the representative red luminophore $[Ru(bpy)_3]^{2+}$ as a case, the luminescence process can be elucidated as a stage involving electron transfer, excited state formation, and radioluminescence.[13,19,21] The specific process is illustrated in Figure 4d: i) before the application of AC bias, the luminescent material dispersed in [EMIM][TFSI] is evenly distributed; ii) upon the application of an electric potential, $[Ru(bpy)_3]^{2+}$ is driven toward the two electrodes to establish an electric double layer (EDL), leading to the generation of the redox luminescent material. The reaction process is as follows:

$$\text{Reduction}: \ Ru(bpy)_3^{2+} + e^- \rightarrow Ru(bpy)_3^{1+} \ (\text{Cathode}) \quad (6)$$

$$\text{Oxidation}: \ Ru(bpy)_3^{2+} - e^- \rightarrow Ru(bpy)_3^{3+} \ (\text{Anode}) \quad (7)$$

Taking one of the electrodes as an example, the distribution of luminophores in the vicinity of the electrode with a negative bias applied is shown in the schematic. (iii) Slow diffusion of reduced luminophores produced at the cathode. When the applied potential on the electrode is changed to be positive, the oxidized luminophores are produced much faster than the diffusion of the original reduced luminophores, and the two are compounded to undergo electron transfer. (iv) A pair of luminophores in the ground and excited states is produced by an annihilation reaction:

$$\text{Annihilation}: \ Ru(bpy)_3^{1+} + Ru(bpy)_3^{3+} \rightarrow Ru(bpy)_3^{2+} + \left[Ru(bpy)_3^{2+}\right]^* \quad (8)$$

here $[Ru(bpy)_3{}^{2+}]^*$ is the excited emitter. The excited luminophore has the following emission:

$$\text{Light emission}: \left[Ru(bpy)_3^{2+}\right]^* \rightarrow Ru(bpy)_3^{2+} + h\nu \quad (9)$$

Eventually, the luminescent entity transitions back to its ground state, emitting photon energy $h\nu$ in. Thus, excitation luminescence occurs at the AC bias without being limited by the electrode's work function. Simultaneously, the reduced $Ru(bpy)_3{}^{1+}$ and oxidized $Ru(bpy)_3{}^{3+}$ migrate toward the electrode and bulk due to concentration gradients, reaching a state of relative equilibrium. The photoluminescence (PL) spectrum of the electrospinning luminescent layer is depicted in Figure 4e. The PL spectra exhibit broad emission peaks, with the most intense peaks at 611 and 528 nm for the red and green samples, respectively. In addition to exciting the luminescent layer, an AC bias was applied to the device to compare ECLD luminescence with and without parylene vaporization (Figure S10, Supporting Information). The design mask plate displayed the letters "G" and "X". Figure S10a (Supporting Information) illustrates the device without parylene vaporization, where the gold-plated layers are clustered in discontinuous islands, resulting in uneven luminescence. Figure S10b (Supporting Information) demonstrates that the inclusion of a parylene intermediate layer results in a more consistent and uniform overall luminescence, preventing image distortion.

ECLDs were fabricated using electrospinning and gel electrolytes. The stress-strain test results presented in Figure S11 (Supporting Information) compare the mechanical properties of devices with these two luminescent layers. Both sets of devices exhibit excellent stretchability, with the electrospinning silk device showing nearly double the elongation at break compared to the gel device, indicating superior mechanical tensile performance. There's no separation of the electrospinning layer and the electrode layer during stretching, and the strong interfacial adhesion provided the basis for the electrical and optical properties to remain insensitive to strain. Figure 4f illustrates the comparison of relative resistance changes in electrospinning and gel devices with a ϵ_{pre} of 50% at various stretching rates. The electrospinning devices exhibit a consistent resistance signal $\Delta R/R_0$ at slightly above ϵ_{pre} (60%). In contrast, the gel devices exhibited a progressive increase in relative resistance until the stretching rate reached ϵ_{pre} (40%), and the rate of change surpassed 100% at 80% strain. Correspondingly, the $\Delta R/R_0$ of the electrospinning device experienced a change of less than 40% at the same 80% strain, indicating the electrical stability of the stretchable electrospinning device. The inset depicts the electrospinning device before and after stretching, revealing no occurrence of interlayer detachment throughout the stretching process.

2.5. Properties and Applications of ECLD

Figure 5a illustrates the electroluminescence (EL) spectra of the ECLD, displaying prominent EL emission peaks at 615 and 551 nm. These peaks closely resemble the PL spectra. However, the presence of semi-transparent gold at the top electrode introduces a slight deviation in the results. The colors represented in the EL spectra were further analyzed and plotted on the CIE-1931 chromaticity diagram in Figure 5b, revealing chromatic coordinates of (0.4689, 0.3507) and (0.3584, 0.4477). These coordinates align with the expected ranges of red-orange and yellow-green luminescence, respectively. The inset shows the corresponding light–emitting device. Analysis of the normalized EL spectra of ECLD-R at peak-to-peak voltages (V_{pp}) ranging from 6 to 11 V (Figure 5c), revealed that the luminescence intensity increased with higher voltages, while the central wavelength remained constant, regardless of the varying AC bias voltages applied. Device test results corresponding to different luminescent solution ratios prove that the wavelength and corresponding color are adjustable under different AC biases (Figures S12 and S13, Supporting Information). Figure 5d provides a detailed comparison of the modulation effect of different concentrations of luminescent solutions on the brightness of luminescence within the V_{pp} range of 0–17 V. In the interval of 0–6 V, the luminous intensity of the ECLD exhibits a gradual increase, almost invisible to the naked eye. As V_{pp} approaches the midpoint of the operational voltage range, the luminous intensity experiences a rapid escalation with the increment of the applied bias voltage until reaching a state of saturation. Upon surpassing the operational voltage threshold, the ECLD momentarily emits a brilliant glow that swiftly diminishes, indicative of an overexertion of the requisite voltage for sustaining the reaction, consequently resulting in a deterioration of the device. Therefore, to ensure the service life,

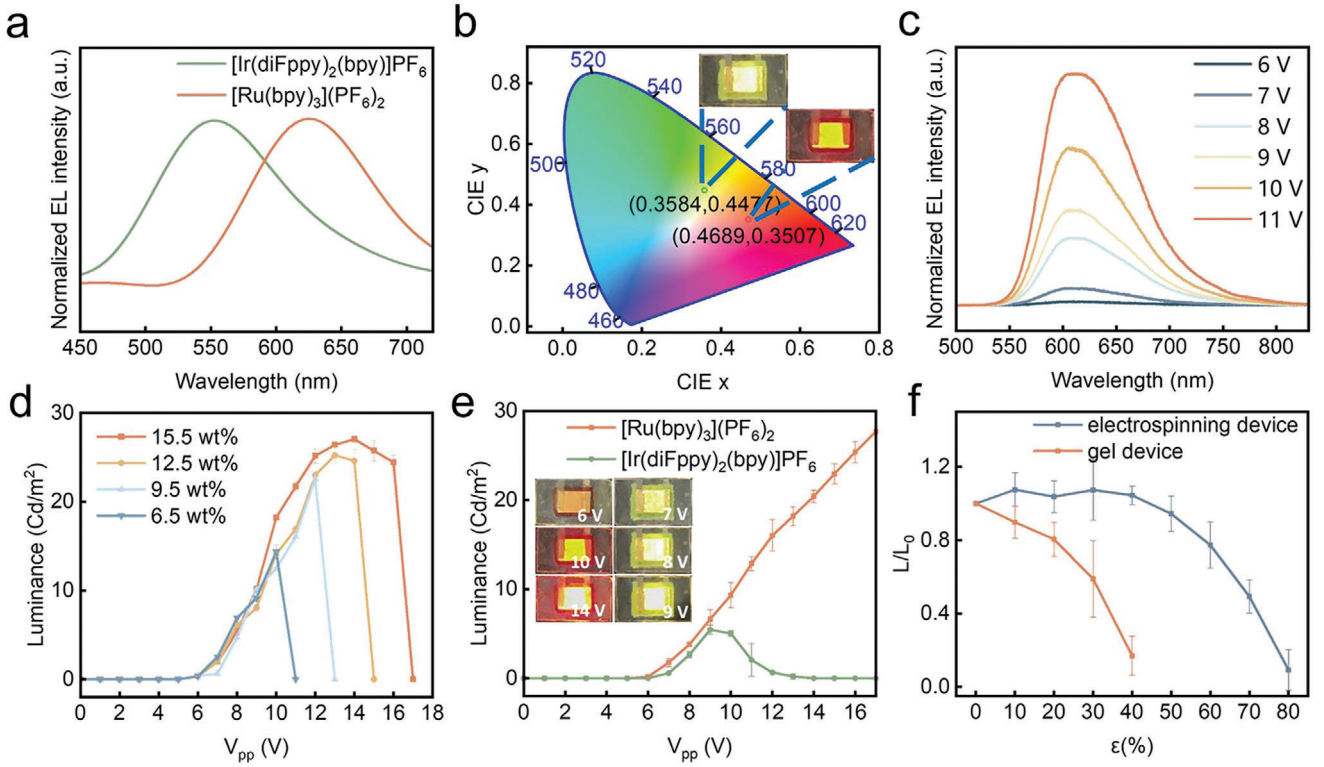

Figure 5. Properties of ECLD. a) EL spectrum of ECLD with red and green emission. b) CIE 1931 chromaticity diagram of the ECLD with red and green emission. c) EL spectrum of ECLD (red) under different applied AC bias. d) Luminance of the ECLD as a function of applied AC bias under different concentration of luminescent solution. e) Luminance of the ECLD with red and green emission as a function of the applied AC bias. f) Luminance of ECLD with electrospinning and gel during stretching as a function of strain.

it is necessary to limit the range of applied voltage, which is also conducive to the stability in maintaining long-term operation.

As the luminophore concentration increases from 6.5 to 15.5 wt.%, the operating voltage range of the ECLD continues to expand and the brightness increases. At concentrations between 12.5 and 15.5 wt.%, the peak brightness shows a gradual increase, while concentrations exceeding 12.5 wt.% lead to the precipitation of particles on the electrospinning layer's surface, hindering further enhancement of the luminophore concentration. Thus, the concentration of luminophore is maintained at 12.5 wt.%, and the luminous brightness of ECLD-R and ECLD-G is ultimately regulated by adjusting the luminous frequency under 100 Hz square wave (Figure 5e; Figure S14 and Movie S1, Supporting Information). When the operating voltage is significantly lower than that of traditional ACELDs, the maximum brightness of ECLD-R is 27.69 Cd m^{-2}, while the luminous efficiency of ECLD-G is notably lower at 5.46 Cd m^{-2}. The inset displays the luminous photographs of ECLD-R and ECLD-G at various bias voltages. Figure 5f compares the brightness of the gel and electrospinning devices at different stretching rates (ϵ_{pre} both set as 50%). The electrospinning device exhibits a slight increase in brightness within a 10% strain range at the beginning of stretching, relative to its initial brightness. This phenomenon can be attributed to improved layer-to-layer contact resulting from stretching at lower strains. At strains ranging from 10% to 50%, the electrospinning devices can maintain luminescence brightness above 80% of the initial level within the ϵ_{pre} range, due to stretchable electrodes with strain-insensitive resistance and an intermediate luminescent layer that exhibits strong adhesion to the electrodes. In contrast, the brightness of gel devices exhibiting the same ϵ_{pre} diminishes progressively, reaching only 20% of the initial brightness at a strain of 40%. This decline is attributed to the non-uniform surface of the gel, as well as its lower viscosity compared to the electrospinning layer, resulting in suboptimal contact with the electrode layer. Conversely, the rough and porous structure of the electrospinning layer allows for better contact and performance. So, we use electrospinning devices with better performance in all of our application sections.

Figure 6a illustrates the comparison of ECLD before and after 40% stretching, indicating that the brightness remains consistent. Through testing mechanical, electrical, and optical signals during stretching, as well as after 500 stretching cycles, the brightness can be maintained over 80% (Figure 6b). The inset displays images of the device at the initial state, 250th cycles, and 500th cycles, respectively. It is demonstrated the stability of the electrospinning ECLD and its potential for stretchable luminescence. Figure 6c is a schematic diagram illustrating the application of the ECLD adhered to human skin, maintaining normal luminescence while following the movement of the skin. To enhance the versatility of applications in two-dimensions, pre-stretching involves the addition of stretching in a direction perpendicular to the original stretching. The presence of anisotropic stresses during multi-directional contraction results in a disordered fold structure Nevertheless, by adjusting the extent of

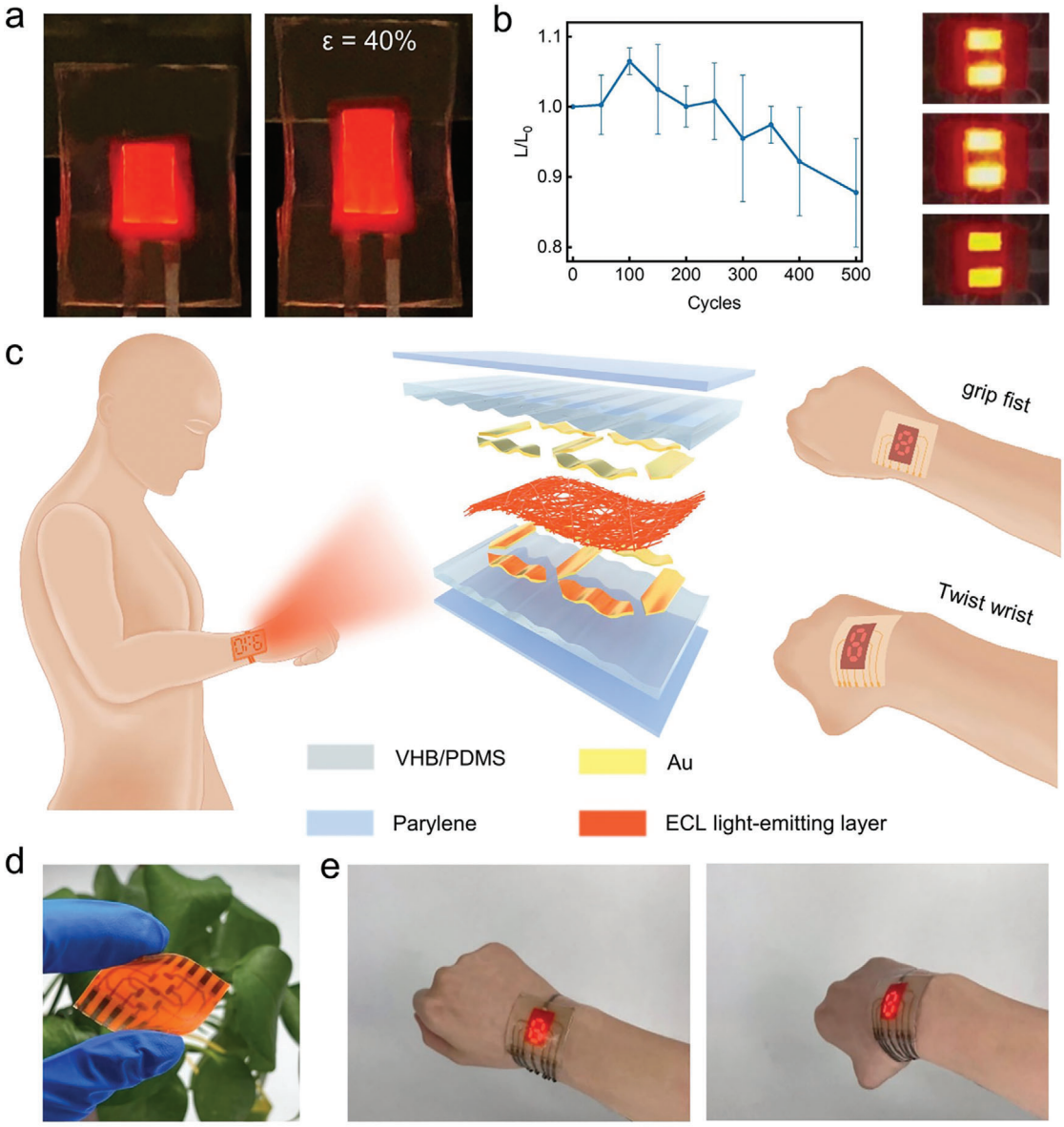

Figure 6. Applications of ECLD. a) Optical photographs of ECLD before and after stretching. b) Luminance of ECLD during stretching as a function of stretching cycles at a strain of 40%. c) Schematic of the applications of ECLD. d) Optical photographs of the ECLD with a single digital tube pattern shown after bending. e) Optical photographs of ECLD including tightly gripping the fist and twisting the wrist.

pre-stretching, we can control the density of folds and implement this approach in the development of expansive, large-area stretchable displays. We prepared a biaxial pre-stretched array, comprising two vertically positioned electrodes arranged in a staggered manner both transversely and vertically to delineate individual pixel points (Figure S15, Supporting Information). In Figure S15a (Supporting Information), a pre-stretched electrode is displayed post-fixation and shrinkage. Figure S15b (Supporting Information) illustrates a 4 × 2 light–emitting array being stretched, with the dynamic process captured in Movie S2 (Supporting Information). Throughout the stretching process, the brightness remains consistently stable.

Further, we apply the ECLD on the human skin to achieve a conformal contact. The display pattern of a wrist-worn watch is simulated, with the seven-segment digitizer determining the display digits. Figure S16 (Supporting Information) shows the mask plate pattern for single- and two-digit tubes, while Figure 6d and Figure S17 (Supporting Information) showcase the prepared ECLDs, highlighting the device's flexibility and uniformity. During the movements involving clenching the fist, extending the arm, and flipping the wrist, the human skin undergoes extension and contraction to maintain stability in brightness. In Figure 6e, Figure S18 and Movie S3 (Supporting Information), all segments of the digital tube are chosen and display the number "8", indicating a complete pathway in each section. The device

maintains a consistent luminous intensity and can illuminate the digital tube to exhibit various numerical values. For instance, the number "6" is displayed by controlling the activation of the seven-segment segment selection. Figure S19 (Supporting Information) illustrates a device on the wrist concurrently showcasing two numerical values, presenting a full display of the number "80". The ECLD, functioning as a wearable device, exhibits strong adhesion to the human skin and maintains operational integrity without delamination when subjected to bending, thereby offering a novel approach for advancing the design of wearable electroluminescent devices powered by low AC voltage.

3. Conclusion

Through in-depth research on electrode design, electrochemical light–emitting layer, device structure and performance of luminescence, we have introduced fully-stretchable display devices based on the ECL principle. The electrode is a metal-polymer composite structure composed of PDMS/VHB/Parylene/Au. Upon strain release, it forms a sinusoidal wrinkled structure, effectively dispersing mechanical strain. The Parylene intermediate layer addresses the modulus matching issue between metal and polymer, balancing the transmittance and surface resistance of the gold-plated electrode. The resistance of the composite structure remains insensitive to strain, ensuring stable relative resistance changes during stretching. Our light–emitting layer features a rough and porous structure achieved through electrospinning, facilitating the uniform infiltration of the luminescent solution. Its photoelectric and mechanical properties surpass those of traditional electrolyte gel. Additionally, the interface between the light–emitting layer and the electrode maintains close contact without delamination occurring during stretching or bending. Crucially, the brightness remains stable. In terms of applications, we have realized a stretchable display of a single pattern and an array. Our ECLD exhibits effective adherence to human skin, allowing it to seamlessly follow the body's movements such as clenching a fist, extending the arm, twisting the wrist, while maintaining stable display brightness. Above all, as a new type of flexible light–emitting device, ECLD combines the unique advantages of electrochemical luminescence with the mechanical properties of stretchable materials. It benefits for easy preparation, simple structure, and large-area preparation at low cost. Our work provides a new strategy for future fully-stretchable display driven by low AC bias.

4. Experimental Section

Materials: Polydimethylsiloxane (PDMS, Sylgard 184) was purchased from Dow Corning. VHB (300 µm) was purchased from 3 M Co., Ltd. Thermoplastic polyurethanes (TPU) pellets (75A) were purchased from Evermore Chemical Industry, Co., Ltd. Polyethylene glycol (PEG, average Mw 400),N,N-dimethylformamide (DMF, 99.9%) and tetrahydrofuran (THF, 99%) were purchased from Shanghai Aladdin Biochemical Technology Co., Ltd. Acetone (CH_3COCH_3, 99.5%) was purchased from Xilong Scientific Co., Ltd. Tris(2,2′-bipyridine)ruthenium(II) hexafluorophosphate ($[Ru(bpy)_3](PF_6)_2$ (99%)), (2,2′-Bipyridine)bis[2-(2,4-difluorophenyl)pyridine]iridium(III) hexafluorophosphate ($[Ir(diFppy)_2(bpy)]PF_6$ (97%)) and 1-ethyl-3-methylimidazolium bis((trifluoromethyl)sulfonyl)imide ([EMIM][TFSI]) were purchased from Shanghai Bide Pharmatech Co., Ltd. All of the materials were used as received.

Fabrication of the Pre-stretched Wrinkled Electrodes: First, the elastomer and crosslinker of PDMS were mixed in a 10:1 weight ratio and the mixture was spin-coated onto a glass using a rotary coater and dried at 70 °C for 2 h. The cured PDMS films were obtained and then peeled off and cut into strips. The VHB strips were cut into the same shape and pasted onto the PDMS strips. Then the whole films were pre-stretched by different strains from 0% to 50%. PET masks were attached to the surface to obtain different patterns. Next, a 1-µm-thick parylene-C layer was deposited on the pre-stretched films using CVD (MQP-3001, Maggie Nano Technology Co., Ltd.). A thin layer of gold was deposited on the parylene layer by magnetron sputtering (PVD75, Kurt J. Lesker, Ar, 70 W) at different times. After strain release, the PDMS/VHB/Parylene/Au wrinkled electrodes were prepared.

Fabrication of the ECLD: The TPU pellets were first dissolved in a solvent with a 1:1 weight ratio of DMF and THF and stirred at 80 °C overnight. Subsequently, the solution was placed in a syringe for electrostatic spinning at a rate of 1.2 mL h^{-1}. The TPU nanofibers were obtained and cut into rectangles with sides of 3 cm × 2 cm. As an example, $[Ru(bpy)_3](PF_6)_2$(0.2 g), [EMIM][TFSI](1.4 g) were mixed into acetone(2.4 g) and stirred at 60 °C until completely dissolved. At the same time, the ratios were adjusted to obtain solutions with different contents of luminophores. Next, the above solutions were immersed into the TPU nanofibers, and after being completely infiltrated, the nanofibers were put into a vacuum-drying oven overnight to remove the organic solvent. At last, the dried ECL nanofibers were sandwiched between two layers of pre-stretched wrinkled electrodes, relying on the adhesion of the VHB strips without an extra spacer. Finally, the whole devices were encapsulated with commercial medical PU tapes (Cofoe Medical Technology Co., Ltd.).

Characterization: The micromorphology of the wrinkled electrodes was characterized by the field-emission scanning electron microscope (FEI Nova NanoSEM 450 and SU8020 Hitachi). The electrical response of electrodes and devices during the stretching process was recorded by an electrochemical workstation (Autolab PGSTAT302N Metrohm) and an LCR meter (E4980A, Agilent). The UV–vis–NIR spectrophotometer (UV-3600 Shimadzu) was used to characterize the transmittance of electrodes. The PL spectra of ECL nanofibers were characterized by a fluorescence spectrometer (FLS980-S2S2-STM), and the EL spectra of devices were characterized by a fiber optic spectrometer (Ocean QE65 Pro). The mechanical performances of electrodes and devices were characterized using the peel strength tester (YL-S70) with a stretching rate of 50 mm min^{-1}. Meanwhile, to test mechanical stability, the electrodes and devices were applied at a dynamic loading of 50% strain by a linear motor.

Supporting Information

Supporting Information is available from the Wiley Online Library or from the author.

Acknowledgements

The authors thank the support of the National Natural Science Foundation of China (No. 52125205, 52250398, U20A20166, 52192614, and 52003101), the National Key R&D Program of China (2021YFB3200300), The Natural Science Foundation of Beijing Municipality (2222088), The Shenzhen Science and Technology Program (Grant No. KQTD20170810105439418) and the Fundamental Research Funds for the Central Universities.

Conflict of Interest

The authors declare no conflict of interest.

Data Availability Statement

The data that support the findings of this study are available from the corresponding author upon reasonable request.

Keywords

conformal wrinkle, electrochemiluminescence, fully-stretchable, polymer-gold, wearable displays

Received: April 16, 2024
Revised: May 10, 2024
Published online:

[1] a) M. Ahmad, Rafi-Ud-Din, C. P., J. Zhu, *J. Phys. Chem. C* **2010**, *114*, 2560; b) X. Wen, W. Wu, C. Pan, Y. Hu, Q. Yang, Z. L. Wang, *Nano Energy* **2015**, *14*, 276; c) R. Zhou, G. Hu, R. Yu, C. Pan, Z. L. Wang, *Nano Energy* **2015**, *12*, 588; d) C. Wang, L. Dong, D. Peng, C. Pan, *Adv. Intell. Syst.* **2019**, *1*, 1900090; e) G. Gao, J. Yu, X. Yang, Y. Pang, J. Zhao, C. Pan, Q. Sun, Z. L. Wang, *Adv. Mater.* **2019**, *31*, 1806905; f) Y. Qi, Y. Liu, C. Lin, Y. Deng, P. Bai, Y. Gao, H. Zhu, Z. Ye, Y. Jin, *J. Materiomics* **2023**, *9*, 762.

[2] a) M. Que, W. Guo, X. Zhang, X. Li, Q. Hua, L. Dong, C. Pan, *J. Mater. Chem. A* **2014**, *2*, 13661; b) L. Zhu, L. Wang, C. Pan, L. Chen, F. Xue, B. Chen, L. Yang, L. Su, Z. L. Wang, *ACS Nano* **2017**, *11*, 1894; c) Y. Lu, X. Qu, W. Zhao, Y. Ren, W. Si, W. Wang, Q. Wang, W. Huang, X. Dong, *Research* **2020**, *2020*, 2038560; d) Y. Liang, Q. Lu, W. Wu, Z. Xu, H. Lu, Z. He, Y. Zhu, Y. Yu, X. Han, C. Pan, *Small Methods* **2023**, *7*, 2300339.

[3] a) G. Ge, W. Yuan, W. Zhao, Y. Lu, Y. Zhang, W. Wang, P. Chen, W. Huang, W. Si, X. Dong, *J. Mater. Chem. A* **2019**, *7*, 5949; b) G. Ge, Y. Lu, X. Qu, W. Zhao, Y. Ren, W. Wang, Q. Wang, W. Huang, X. Dong, *ACS Nano* **2020**, *14*, 218; c) J. Tao, M. Dong, L. Li, C. Wang, J. Li, Y. Liu, R. Bao, C. Pan, *Microsyst. Nanoeng.* **2020**, *6*, 62; d) K. Zhou, Y. Zhao, X. Sun, Z. Yuan, G. Zheng, K. Dai, L. Mi, C. Pan, C. Liu, C. Shen, *Nano Energy* **2020**, *70*, 104546; e) K. Zhou, W. Xu, Y. Yu, W. Zhai, Z. Yuan, K. Dai, G. Zheng, L. Mi, C. Pan, C. Liu, C. Shen, *Small* **2021**, *17*, 2100542.

[4] a) X. Han, Z. Xu, W. Wu, X. Liu, P. Yan, C. Pan, *Small Struct* **2020**, *1*, 2000029; b) C. Wang, R. Ma, D. Peng, X. Liu, J. Li, B. Jin, A. Shan, Y. Fu, L. Dong, W. Gao, Z. L. Wang, C. Pan, *InfoMat* **2021**, *3*, 1272; c) W. Wu, X. Han, J. Li, X. Wang, Y. Zhang, Z. Huo, Q. Chen, X. Sun, Z. Xu, Y. Tan, C. Pan, A. Pan, *Adv. Mater.* **2021**, *33*, 2006006; d) J. Sun, T. Li, L. Dong, Q. Hua, S. Chang, H. Zhong, L. Zhang, C. Shan, C. Pan, *Sci. Bull.* **2022**, *67*, 1755; e) C. Wang, H. Hu, D. Zhu, C. Pan, *Sci. Bull.* **2023**, *68*, 559; f) W. Wu, H. Lu, X. Han, C. Wang, Z. Xu, S. T. Han, C. Pan, *Small Methods* **2023**, *7*, 2201499.

[5] D. Won, J. Bang, S. H. Choi, K. R. Pyun, S. Jeong, Y. Lee, S. H. Ko, *Chem. Rev.* **2023**, *123*, 9982.

[6] N. Kaiser, *Appl. Optics* **2002**, *41*, 3053.

[7] H. Kang, S. Jung, S. Jeong, G. Kim, K. Lee, *Nat. Commun.* **2015**, *6*, 6503.

[8] a) D. Park, S. J. Shin, T. S. Oh, *J. Electron. Mater.* **2017**, *47*, 9; b) H. Moon, J.-W. Jang, S. Park, J.-H. Kim, J. S. Kim, S. Kim, *Sens. Actuator B-Chem.* **2024**, *401*, 135099.

[9] a) F. Li, X. Wang, Z. Xia, C. Pan, Q. Liu, *Adv. Funct. Mater.* **2017**, *27*, 1700051; b) J.-W. P. Jin-Hoon Kim, *Sci. Adv.* **2021**, *7*, eabd9715; c) Z. Y. Chen, Z. K. Ji, D. Yin, Y. F. Liu, Y. G. Bi, J. Feng, H. B. Sun, *Adv. Mater. Tech.* **2022**, *7*, 2101263; d) T. Meng, Y. Zheng, D. Zhao, H. Hu, Y. Zhu, Z. Xu, S. Ju, J. Jing, X. Chen, H. Gao, K. Yang, T. Guo, F. Li, J. Fan, L. Qian, *Nat. Photonics* **2022**, *16*, 297; e) M. Jiang, X. Zhang, F. Wang, *Nano Res. Energy* **2023**, *2*, 9120069; f) D.-G. Zheng, H.-D. Lee, G. W. Lee, D.-S. Shin, J. Kim, J.-I. Shim, Z. Lin, T.-W. Lee, D. H. Kim, *Nano Res. Energy* **2024**, *3*, 9120109; g) S. Zheng, X. Mei, J. Chen, E. M. J. Johansson, X. Zhang, *Nano Res. Energy* **2024**, *3*, 9120095.

[10] a) D. W. Kim, G. Lee, M. Pal, U. Jeong, *ACS Appl. Mater. Interfaces* **2020**, *12*, 41969; b) W. Jiang, S. Lee, G. Zan, K. Zhao, C. Park, *Adv. Mater.* **2023**, *36*, 2304053.

[11] X. Shi, Y. Zuo, P. Zhai, J. Shen, Y. Yang, Z. Gao, M. Liao, J. Wu, J. Wang, X. Xu, Q. Tong, B. Zhang, B. Wang, X. Sun, L. Zhang, Q. Pei, D. Jin, P. Chen, H. Peng, *Nature* **2021**, *591*, 240.

[12] P. Zhang, I. M. Lei, G. Chen, J. Lin, X. Chen, J. Zhang, C. Cai, X. Liang, J. Liu, *Nat. Commun.* **2022**, *13*, 4775.

[13] K. G. Cho, J. I. Lee, S. Lee, K. Hong, M. S. Kang, K. H. Lee, *Adv. Funct. Mater.* **2020**, *30*, 1907936.

[14] a) J. H. Kwon, Y. M. Kim, H. C. Moon, *ACS Nano* **2021**, *15*, 15132; b) D. Zhang, X. Meng, W. Hou, W. Hu, J. Mo, T. Yang, W. Zhang, Q. Fan, L. Liu, B. Jiang, L. Chu, M. Li, *Nano Res. Energy* **2023**, *2*, 9120050.

[15] Z. Zhang, W. Wang, Y. Jiang, Y.-X. Wang, Y. Wu, J.-C. Lai, S. Niu, C. Xu, C.-C. Shih, C. Wang, H. Yan, L. Galuska, N. Prine, H.-C. Wu, D. Zhong, G. Chen, N. Matsuhisa, Y. Zheng, Z. Yu, Y. Wang, R. Dauskardt, X. Gu, J. B. H. Tok, Z. Bao, *Nature* **2022**, *603*, 624.

[16] J. I. Lee, H. Choi, S. H. Kong, S. Park, D. Park, J. S. Kim, S. H. Kwon, J. Kim, S. H. Choi, S. G. Lee, D. H. Kim, M. S. Kang, *Adv. Mater.* **2021**, *33*, 2100321.

[17] D.-K. Kwon, J.-M. Myoung, *ACS Nano* **2020**, *14*, 8716.

[18] J.-W. Oh, J.-Y. Jeong, T.-Y. Eom, S.-D. Baek, J.-M. Myoung, *Chem. Eng. J.* **2021**, *416*, 129202.

[19] K. Hong, Y. K. Kwon, J. Ryu, J. Y. Lee, S. H. Kim, K. H. Lee, *Sci. Rep.* **2016**, *6*, 29805.

[20] J. H. Song, Y. T. Kim, S. Cho, W. J. Song, S. Moon, C. G. Park, S. Park, J. M. Myoung, U. Jeong, *Adv. Mater.* **2017**, *29*, 1702625.

[21] D.-K. Kwon, J.-M. Myoung, *Chem. Eng. J.* **2020**, *379*, 122347.

[22] H. Yin, Y. Zhu, K. Youssef, Z. Yu, Q. Pei, *Adv. Mater.* **2021**, *34*, 2106184.

[23] R. Bao, J. Tao, J. Zhao, M. Dong, J. Li, C. Pan, *Sci. Bull.* **2023**, *68*, 1027.

[24] W. Gao, J. Huang, J. He, R. Zhou, Z. Li, Z. Chen, Y. Zhang, C. Pan, *InfoMat* **2023**, *5*, e12426.

[25] R. Zhou, Y. Zhang, F. Xu, Z. Song, J. Huang, Z. Li, C. Gao, J. He, W. Gao, C. Pan, *Small* **2023**, *19*, 2301544.

[26] J. He, R. Zhou, Y. Zhang, W. Gao, T. Chen, W. Mai, C. Pan, *Adv. Funct. Mater.* **2021**, *32*, 2107281.

[27] R. Yang, H. Song, Z. Zhou, S. Yang, X. Tang, J. He, S. Liu, Z. Zeng, B.-R. Yang, X. Gui, *ACS Appl. Mater. Interfaces* **2023**, *15*, 8345.

[28] S. Hou, C. Chen, L. Bai, J. Yu, Y. Cheng, W. Huang, *Small* **2023**, *20*, 2306749.